Proceedings of ASME Turbo Expo 2011
GT2011
June 6-10, 2011, Vancouver, British Columbia, Canada

GT2011-46510

MEASURED AND PREDICTED TRANSFER FUNCTIONS BETWEEN ROTOR MOTION AND PAD MOTION FOR A ROCKER-BACK TILTING-PAD BEARING IN LOP CONFIGURATION

Jason C. Wilkes
Graduate Research Assistant,
jasonwilkes@tamu.edu
Turbomachinery Laboratory, Texas A&M University,
College Station, TX, 77802, USA

ABSTRACT

Many researchers have compared predicted stiffness and damping coefficients for tilting-pad journal bearings (TPJBs) to measurements. Most have found that direct damping is consistently overpredicted. Continuing to test TBJBs in the same fashion is not likely to produce an explanation for the discrepancies between measured and predicted damping. Most analytical models for TPJBs are based on the assumption that explicit dependence on pad motion can be eliminated by assuming a solution for rotor motion such that the amplitude and phase of pad motions are predicted by rotor-pad transfer functions. Direct measurements of pad motion during test excitation are needed to produce measured transfer functions between rotor and pad motion, and a comparison between these measurements and predictions is needed to identify model discrepancies.

A test setup was designed to fulfill these objectives. Motion probes were added to the loaded pad to obtain accurate measurement of pad radial and tangential motion, as well as tilt, yaw and pitch. For the remainder of this work, the loaded pad refers to the pad whose pivot sits on the static load line. Testing was performed primarily at low speeds and high loads, since this is the operating region for which predictions are most erroneous. Single frequency excitations were performed ranging from 10-350 Hz, producing rotor and pad motion, acceleration, and force vectors. This motion was used to determine frequency-dependent bearing impedances and rotor-pad transfer functions.

A new pad perturbation model is proposed including the effects of pad angular, radial, and circumferential pad motion. This model was implemented in a Reynolds-based TPJB code to predict the frequency-dependent bearing impedances and rotor-pad transfer functions. These predictions are compared with measurements and discussed.

Good agreement was found between the amplitude of the measured and predicted transfer functions concerning tilt and radial motions for low to moderate loads, but deviated in accuracy at the highest loaded case. Circumferential (sliding) pad motion was predicted and observed; however, the effect of this degree of freedom on dynamic bearing coefficients has not been quantitatively assessed.

For the bearing investigated, radial motion accounted for more than 67% of total motion of the fluid-film height at the leading and trailing edges of the pad when operating at 4400 rpm under heavily loaded conditions. The measurements show that predicting TPJB stiffness and damping coefficients without accounting for pad pivot deformation will not produce satisfactory outcomes.

INTRODUCTION

In the history of TPJBs, few additions to literature have been more significant than those by Lund [1] in 1964 and Lund and Pederson [2] in 1987. The former outlined a method for the calculation of stiffness and damping coefficients for a TPJB. Procedurally, Lund solves for static equilibrium, perturbs the pad equation of motion, eliminates the system's explicit dependence on pad motion by assuming harmonic rotor motion, and calculates direct and cross-coupled stiffness and damping coefficients for the bearing. Lund assumes that rotor motion is harmonic in the perturbation/ reduction frequency Ω, and that running speed ω is an appropriate choice for Ω. This choice of reduction frequency, termed to be a 'synchronous reduction,' does not limit Lund's analysis to the determination of synchronous coefficients, and should not be portrayed as such. This frequency choice has been a subject of much discussion over the past few decades. In the latter work, Lund and Pederson reflect upon the original assumption of rotor motion and state, "In the special case of a damped eigenvalue calculation or a rotor stability calculation, the frequency term, $j\Omega$, **must** be replaced by the complex eigenvalue: $s=\lambda+j\Omega$, where λ is the damping exponent." Lund and Pederson also include a perturbation of film height due to pivot flexibility and pad deformation, which reduces the stiffness and damping of the bearing, especially the latter. These findings were supported by Barrett et al. [3] who illustrate the importance of using system eigenvalues for stability assessment. Barrett et al. retains the full damped eigenvalue $s=\lambda+j\Omega$ to determine system stability. They conclude that using synchronously reduced coefficients will tend to overestimate stability, especially for a bearing operating at high Sommerfeld numbers and low preloads. Kirk and Reedy [4] supported Lund and Pederson's conclusions concerning pivot stiffness, namely that it should be included in the calculation of bearing coefficients. Dmochowski was the first to back up this conclusion with good agreement between experiments and predictions for a model containing support flexibility for the pad [5].

Experimentally, Ha and Yang [6] reported a very slight increase in damping and little or no variation in stiffness with excitation frequency ratio; however, the limited range of excitation frequencies used in these tests is questionable. These effects were more pronounced at lower speeds and higher static loads. Other researchers [5-10] have shown the frequency dependence of measured stiffness data is well approximated by an added mass, initially proposed for hydrostatic bearings by Rouvas and Childs [11], which results in frequency independent stiffness, damping, and mass (KCM) matrices that define the bearing reaction force. This does not imply that the parameter identification procedure used by researchers [5-10] cannot show frequency dependent stiffness and damping, just that the frequency dependent stiffness observed is proportional to Ω^2, which is adequately included by the addition of an 'added-mass' term in the bearing reaction force model. The added-mass terms presented are usually relatively small (5-10kg), and typically have a softening effect; however, some researchers have shown added mass terms that have a stiffening effect [8,12-13]. While Dmochowski [5] shows a small decrease in damping with excitation frequency, other researchers [7-13] found damping to be constant with excitation frequency.

With a few exceptions, experimental measurement of *pad* motion has typically been limited to the observation of pad flutter on unloaded pads. Sabnavis [14] attempts to measure pad motion of a spherical seat TPJB, but fails to produce meaningful phase and amplitude measurements.

The current work will address the issue of frequency dependency in TPJBs by investigating the assumptions made in the prediction and measurement of TPJB dynamic coefficients.

NOMENCLATURE

FFT	Fast-Fourier Transform	
KCM	Stiffness, Damping, and Mass	
TPJB	Tilting-Pad Journal Bearing	
C.G.	Center of Gravity	
A_x,A_y	Acceleration of the stator	m/s^2
$\boldsymbol{A_{ij}}$	Complex Equation of Motion	m (in)
C_b	Radial Bearing Clearance	m (in)
C_{pk}	Pivot Damping in direction k	N.s/m (lb.s/in)
dF_k	Differential Force along k	N (lb)
H_{ij}	Complex Bearing Impedance	
F_x,F_y	Applied force to the Stator	N (lb)
I_{ij}	Fixed impedance $I_{ij} = \left(K_{ij} + sC_{ij}\right)$	
I_o	Pad Inertia about Pivot	kg-m^2 (lb.s^2.in)
K_{pk}	Pivot Stiffness in direction k	N/m (lb/in)
$M_{11\text{-}15}$	Raw Pad Probe Displacements	m (in)
$\mathbf{M_{jj}}$	Journal Mass Matrix	kg (lb.s^2/in)
O_p,O_j	Geometric Center of Pad, Journal	m (in)
$\boldsymbol{Q}$	Direction Cosine Matrix	
R	Radius	m (in)
U_j, U_p	Complex Journal/Pad Motions	m (in)
X, Y, Z	Inertial Coordinate Frame	
X_g,Y_g	Pad Center of Gravity	m (in)
X_p,Y_p	Pad Pivot Motion from Equilibrium	m (in)
j	Imaginary Unit $j = \sqrt{-1}$	-
m_p	Mass of Pad	kg (lb.s^2/in)
m_r, m_s	Rotor/Stator Mass	kg (lb.s^2/in)
p_x,p_y	Distance from Pivot to pad C.G.	m (in)
s	Assumed Complex Root $s= \lambda+j\Omega$	
t	Time	s
$\boldsymbol{\Gamma}$	Rotor-pad Transfer Function	
Ω	Data reduction/perturbation frequency	rad/sec
α	Angle from X-axis ξ_p	rad
ζ	System damping ratio	
η,ξ	Differential motion between the rotor and stator along the η,ξ pad axis	m (in)
λ	Damping exponent, $\lambda=-\zeta\Omega_n$	
ϕ	Pad tilt angle	rad
ϕ_{Xp},ϕ_{Yp}	Pad tilt angle about X_p, Y_p	rad
ω	Running speed	rad/sec

Subscripts

x,y	Inertial Rotor Frame
j	Journal
c	Contact
b	Bearing
p	Pivot/Pad
η,ξ	Pad fixed frame

MATHEMATICAL MODEL

The important parameters in the pad perturbation model are shown in Figure 1. The pad shown is free to tilt an angle ϕ about the bearing's Z axis, while the pivot can translate in the radial and circumferential directions along axes Y and X, respectively. Previous researchers have neglected pad motion in the circumferential direction.

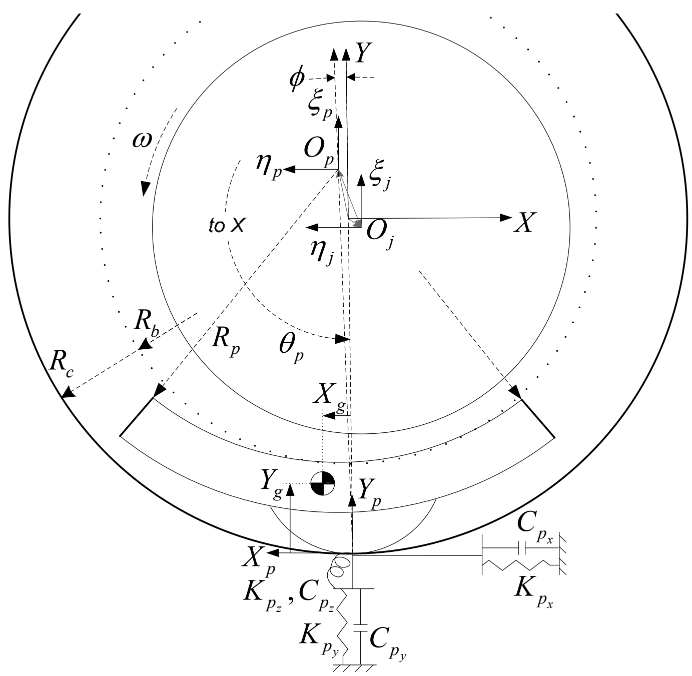

Figure 1: Schematic of the pad perturbation model

As proposed by Lund [1], the change in reaction force between the rotor and pad due to differential motion from equilibrium for a single pad is given by

$$\begin{aligned} dF_\xi &= -K_{\xi\xi}\xi - C_{\xi\xi}\dot{\xi} - K_{\xi\eta}\eta - C_{\xi\eta}\dot{\eta} \\ dF_\eta &= -K_{\eta\xi}\xi - C_{\eta\xi}\dot{\xi} - K_{\eta\eta}\eta - C_{\eta\eta}\dot{\eta} \end{aligned}, \tag{1}$$

where

$$\begin{aligned} &\eta = \eta_j - \eta_p,\ \ \dot{\eta} = \dot{\eta}_j - \dot{\eta}_p,\ \ \xi = \xi_j - \xi_p,\ \ \dot{\xi} = \dot{\xi}_j - \dot{\xi}_p, \\ &\eta_p = X_p + R_{co_p}\phi,\ \ \dot{\eta}_p = \dot{X}_p + R_{co_p}\dot{\phi},\ \ \xi_p = Y_p,\ \ \dot{\xi}_p = \dot{Y}_p \end{aligned}. \tag{2}$$

The angle of rotation (tilt) of the pad from its equilibrium position is ϕ, and R_{co_p} is the distance from the pivot contact point to the center of the pad given by $R_{co_p} = R_p + R_c - R_b = R_p + t_{rp}$, where R_p, R_c, and R_b are the pad, contact, and bearing radii, and t_{rp} is the thickness of the pad at the rocker. Pad pivot motions X_p and Y_p denote motion of the pad pivot from equilibrium in the inertial frame. Note that X_p denotes pivot motion along the negative X axis.

The pad's center of gravity (C.G.) located in the inertial frame, with the equilibrium contact point taken as a datum, is given by

$$\begin{aligned} &X_g = p_x + p_y\sin(\phi) + X_p,\ \ Y_g = p_y - p_x\sin(\phi) + Y_p, \\ &\dot{X}_g = p_y\cos(\phi)\dot{\phi} + \dot{X}_p,\ \ \dot{Y}_g = -p_x\cos(\phi)\dot{\phi} + \dot{Y}_p, \\ &\ddot{X}_g = p_y\left(\cos(\phi)\ddot{\phi} - \sin(\phi)\dot{\phi}^2\right) + \ddot{X}_p,\ \ \ddot{Y}_g = -p_x\left(\cos(\phi)\ddot{\phi} - \sin(\phi)\dot{\phi}^2\right) + \ddot{Y}_p \end{aligned}, \tag{3}$$

where p_x and p_y describe the distance from the contact location to the pad's center of mass. Using these relations, the pad's equation of motion is

$$\begin{aligned} &\sum F_{x,p} = m_p\ddot{X}_g = -dF_\eta - K_{p_x}X_p - C_{p_x}\dot{X}_p \\ &\sum F_{y,p} = m_p\ddot{Y}_g = -dF_\xi - K_{p_y}Y_p - C_{p_y}\dot{Y}_p \\ &\sum M_p = I_o\ddot{\phi} - m\left(b_{pg}\times\ddot{R}_{co_p}\right) = I_o\ddot{\phi} + m_p\left(p_y\ddot{X}_p - p_x\ddot{Y}_p\right) = -R_{co_p}dF_\eta - K_{p_z}\phi - C_{p_z}\dot{\phi} \end{aligned}, \tag{4}$$

where $K_{p_x}, C_{p_x}, K_{p_y}, C_{p_y}$, are the tangential and radial contact stiffness and damping, and K_{p_z}, C_{p_z}, are the rotational stiffness and damping at the pivot, respectively. The second term in the moment equation is required because moments are summed about the contact point (X_p, Y_p), which is free to translate. The term b_{pg} describes the vector from the pivot to the pad's C.G. The rotor's equation of motion is similarly given by

$$\begin{aligned} \sum F_{x,j} &= m_j\ddot{X}_j = dF_\eta \\ \sum F_{y,j} &= m_j\ddot{Y}_j = dF_\xi \end{aligned} \tag{5}$$

Assuming that the perturbation is subject to vibration of the form, $(\xi_i,\eta_i) = (\overline{\xi}_i,\overline{\eta}_i)e^{st} = (\overline{\xi}_i,\overline{\eta}_i)e^{(-\lambda+j\Omega)t}$, where s is the complex root of the assumed solution, the differential forces are now

$$\begin{aligned} dF_\xi &= \left[-\left(K_{\xi\xi}+sC_{\xi\xi}\right)\overline{\xi} - \left(K_{\xi\eta}+sC_{\xi\eta}\right)\overline{\eta}\right]e^{st} \\ dF_\eta &= \left[-\left(K_{\eta\xi}+sC_{\eta\xi}\right)\overline{\xi} - \left(K_{\eta\eta}+sC_{\eta\eta}\right)\overline{\eta}\right]e^{st} \end{aligned}, \tag{6}$$

where $\overline{\xi} = \left(\overline{\xi}_j - \overline{Y}_p\right)$, $\overline{\eta} = \left(\overline{\eta}_j - \overline{X}_p - R_{co_p}\overline{\phi}\right)$. Assuming that the change in pad tilt angle ϕ induced by rotor motion is small, the acceleration of the pad's C.G. $\ddot{X}_g, \ddot{Y}_g$ can be linearized as

$$\begin{aligned} \ddot{X}_g &= \left[p_y\left(\cos(\phi) - \sin(\phi)\right)\left(s^2\overline{\phi}\right) + s^2\overline{X}_p\right]e^{st} \cong s^2\left[p_y\overline{\phi} + \overline{X}_p\right]e^{st} \\ \ddot{Y}_g &= \left[-p_x\left(\cos(\phi) - \sin(\phi)\right)\left(s^2\overline{\phi}\right) + s^2\overline{Y}_p\right]e^{st} \cong s^2\left[-p_x\overline{\phi} + \overline{Y}_p\right]e^{st} \end{aligned}. \tag{7}$$

Using Eqs. (1-7), the equations of motion for the system can be given by

$$\left[\begin{array}{cc|ccc} I_{\eta\eta} & I_{\eta\xi} & -R_{co_p}I_{\eta\eta} & -I_{\eta\eta} & -I_{\eta\xi} \\ I_{\xi\eta} & I_{\xi\xi} & -R_{co_p}I_{\xi\eta} & -I_{\xi\eta} & -I_{\xi\xi} \\ \hline -R_{co_p}I_{\eta\eta} & -R_{co_p}I_{\eta\xi} & I_o s^2 + R_{co_p}{}^2 I_{\eta\eta} + I_{p_z} & m_p p_y s^2 + R_p I_{\eta\eta} & -m_p p_x s^2 + R_{co_p}I_{\eta\xi} \\ -I_{\eta\eta} & -I_{\eta\xi} & m_p p_y s^2 + R_{co_p}I_{\eta\eta} & m_p s^2 + I_{\eta\eta} + I_{p_x} & I_{\eta\xi} \\ -I_{\xi\eta} & -I_{\xi\xi} & -m_p p_x s^2 + R_{co_p}I_{\xi\eta} & I_{\xi\eta} & m_p s^2 + I_{\xi\xi} + I_{p_y} \end{array}\right]\left\{\begin{array}{c} \overline{\eta}_j \\ \overline{\xi}_j \\ \overline{\phi} \\ \overline{X}_p \\ \overline{Y}_p \end{array}\right\} = \begin{bmatrix} -m_j s^2\overline{\eta} \\ -m_j s^2\overline{\xi} \\ 0 \\ 0 \\ 0 \end{bmatrix} \tag{8}$$

where

$$\begin{aligned} &I_{\xi\xi} = \left(K_{\xi\xi}+sC_{\xi\xi}\right),\ I_{\xi\eta} = \left(K_{\xi\eta}+sC_{\xi\eta}\right),\ I_{\eta\xi} = \left(K_{\eta\xi}+sC_{\eta\xi}\right),\ I_{\eta\eta} = \left(K_{\eta\eta}+sC_{\eta\eta}\right), \\ &I_{p_z} = \left(K_{p_z}+sC_{p_z}\right),\ I_{p_x} = \left(K_{p_x}+sC_{p_x}\right),\ I_{p_y} = \left(K_{p_y}+sC_{p_y}\right). \end{aligned} \tag{9}$$

For the sake of brevity, Eq. (8) will be rewritten as

$$\begin{bmatrix} \mathbf{A_{jj}} & \mathbf{A_{jp}} \\ \mathbf{A_{pj}} & \mathbf{A_{pp}} \end{bmatrix}\begin{Bmatrix} \mathbf{U_J} \\ \mathbf{U_P} \end{Bmatrix} = \begin{Bmatrix} -\mathbf{M_{jj}}s^2\mathbf{U_J} \\ \mathbf{0} \end{Bmatrix} \tag{10}$$

where the partition in Eq. (8) separates the journal from the pad. Using the bottom set of relations in Eq. (10), we solve for $\mathbf{U_P}$ according to

$$\mathbf{U_P} = -\mathbf{A_{pp}}^{-1}\mathbf{A_{pj}}\mathbf{U_J} = \mathbf{\Gamma_{pj}}\mathbf{U_J}, \tag{11}$$

where $\mathbf{\Gamma_{pj}}$ is the pad-rotor transfer-function matrix. To predict the correct reduced coefficients for a TPJB, this relation must be accurate. Validating this relation by the comparison of measured and predicted rotor-pad transfer functions is a primary goal of this research.

To obtain reduced stiffness and damping coefficients, $\mathbf{U_P}$ is substituted into the top set of relations in Eq. (10) to yield

$$\left(\mathbf{M_{jj}}s^2 + \mathbf{A_{jj}} - \mathbf{A_{jp}}\mathbf{A_{pp}}^{-1}\mathbf{A_{pj}}\right)\mathbf{U_J} = \left(\mathbf{M_{jj}}s^2 + \mathbf{H_{jj}}\right)\mathbf{U_J} = \mathbf{0}. \tag{12}$$

The reduced stiffness and damping coefficients are given by the real and imaginary parts of

$$\mathbf{H_{jj,\mu\xi}} = \begin{bmatrix} \overline{H}_{\eta\eta_{red}} & \overline{H}_{\eta\xi_{red}} \\ \overline{H}_{\xi\eta_{red}} & \overline{H}_{\xi\xi_{red}} \end{bmatrix} = \mathbf{A_{jj}} - \mathbf{A_{jp}}\mathbf{A_{pp}}^{-1}\mathbf{A_{pj}}. \tag{13}$$

The additional subscripts η, ξ indicate that an impedance relates to motions in the pad-fixed frame. The terms in Eq. (13) are rotated into the journal defined coordinate system X_j,Y_j using

$$\mathbf{H_{jj,xy}} = \begin{bmatrix} -\sin(\alpha) & \cos(\alpha) \\ \cos(\alpha) & \sin(\alpha) \end{bmatrix}\mathbf{H_{jj,\mu\xi}}\begin{bmatrix} -\sin(\alpha) & \cos(\alpha) \\ \cos(\alpha) & \sin(\alpha) \end{bmatrix} = \mathbf{Q^T}\mathbf{H_{jj,\mu\xi}}\mathbf{Q}, \tag{14}$$

where $\alpha = \theta_p + \pi$, and Q is the direction cosine matrix from the journal-fixed inertial X-Y frame to the pad-fixed inertial η, ξ frame (η, ξ do not rotate with pad angle ϕ).

This pad-perturbation model is applicable to the reduction of stiffness and damping terms for both damped and undamped (harmonic) motions of the rotor relative to the stator given the proper selection of s.

There are many papers concerning the proper approach to use in the reduction of TPJB stiffness and damping coefficients; the following should serve to as a summary on the matter. For the prediction of stability, Lund and Pederson state that $s=\lambda+j\Omega$. As stated by Barrett et al., λ =0 at the threshold speed of instability, which eliminates the need for stability calculations using a full damped eigenvalue; however, the authors later conclude that employing a damped eigenvalue in the calculation of a reduced stiffness and damping coefficients will tend to reduce the stability of the system, especially for lightly preloaded bearings running at high Sommerfeld numbers [3]. A synchronous reduction is valid for the determination of stiffness and damping of harmonic oscillation such as imbalance response. In the event that the predictions can be adequately modeled by an added-mass term, this is an excellent approach, as it will save both time and effort in eliminating the need to determine the best frequency to use in calculations.

Another method is to employ the full unreduced bearing model in Eq. (8) to determine system stability as done by Qiao et al. [15]. The improvement in stability prediction of this approach over a reduced model has not been adequately addressed for a realistic rotordynamic system.

BEARING AND TEST RIG DESCRIPTION

General Description

A drawing of the test rig is shown in Figure 2.

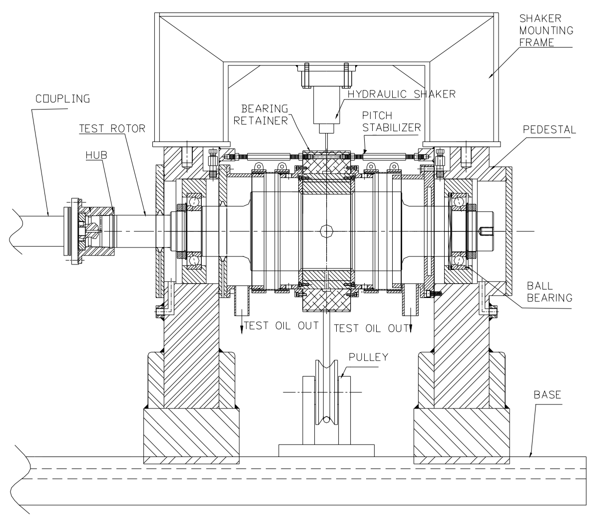

Figure 2: Drawing of the test rig [12]

A thorough description of this test rig is given in [7-9,12], and will not be discussed in detail here. The test rig is a floating-bearing test rig modeled after Glienicke [16], in which a bearing floats on an oil film supported by a 'rigid rotor.' The bearing, or stator, is excited by means of hydraulic actuators at various frequencies while components of applied force, absolute stator acceleration and relative rotor-stator motion vectors are recorded. In addition to dynamic excitations, a static load can be applied up to 22 kN.

Figure 3 shows a picture of the stator with a bearing installed. This picture shows two locations for the proximity probes, one set adjacent to the stinger connections in yellow, and another set 180° away from the stinger connection in red. Previously, the proximity probes were located 180° from the stinger connections, which do not move with the same amplitude and phase as the stinger during the application of dynamic loads due to stator flexibility. The effect of relative motion between the top and bottom was confirmed by the reduction of data simultaneously recorded by probes in both locations. This change in probe orientation has a notable effect on measured impedances, quantified by a 10%-15% decrease in stiffness and a reduction in added-mass. Because most of the dynamic load is carried by the statically loaded pad, more accurate impedance coefficients and loaded pad transfer functions will be obtained by mounting the proximity probes adjacent to the stingers. The current tests were conducted with accelerometers and proximity probes mounted in this configuration, as were full bearing tests by Kulhanek [12] and Kulhanek and Childs [13].

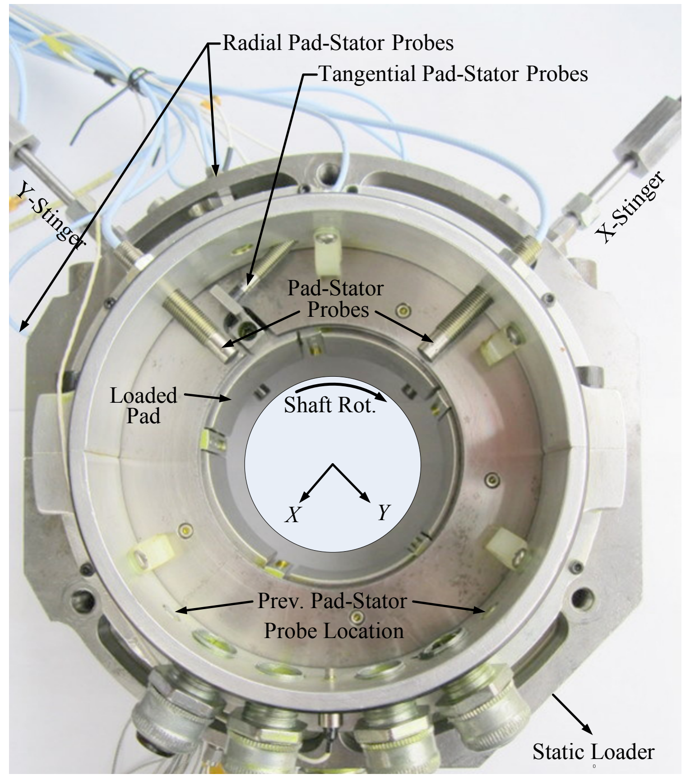

Figure 3: Stator and test bearing viewed from the non-drive end

Test Bearing

A description of the test bearing configuration is given in Table 1. A rocker pivot similar to the one shown in Figure 1 is used. Pads are retained by a loose fitting pin, which allows the pivot to tilt, slide and bounce. X_p and ϕ are independent variables; therefore, no rolling-without-slipping relation is assumed.

Table 1: Properties of the bearing at room temp. (24 °C).

Number of Pads	5
Loading Configuration	LOP
Pad Arc Angle (θ_{01})	58.9
Rotor Diameter	101.587 mm (3.9995 in)
Pad Axial Length	55.88 mm (2.200 in)
Cold Bearing Radial Clearance[1]	68 μm (2.67 mils)
Cold Pad Radial Clearance[1]	120.65 μm (4.75 mils)
Cold Bearing Preload[1]	0.44
Pad Mass	0.44 kg (0.97 lb)
Pad Inertia	2.49e-4 kg-m^2 (0.851 lb-in^2)
Bearing Lubricant	DTE 797, ISO VG-32

Note 1: The cold bearing clearance describes the dimensions of the bearing at room temperature, not at operating conditions. Measurements of clearances and their dependence on temperature will be discussed in the results section.

Test Series

Testing was performed at the operating conditions prescribed in Table 2. Data was taken at 10-350 Hz, in 10 Hz increments.

Table 2: Operating conditions

Static Load	Speed [rpm], (Flow-rate [gpm])		
kPa (psi)	4400, (8)	7300, (8)	10100, (10)
0	x	x	x
783 (113.6)	x	x	x
1567 (227.2)	x	x	x
2350 (340.9)	x	x	x
3134 (454.5)	x		

Pad Instrumentation

The primary degrees of freedom measured on the loaded pad are shown in Figure 4. Each degree of freedom is measured from the equilibrium position of the pad at a given operating condition. Two additional degrees of freedom are measured during tests, but are not shown in the diagram. Pad yaw (ϕ_{Yp}) is defined as the rotation from equilibrium-axis Z_0 to the perturbed axis Z_1 about the positive Y_0-axis, and pad pitch (ϕ_{Xp}) is defined as the rotation from equilibrium-axis Z_0 to the perturbed axis Z_1 about the positive X_0-axis.

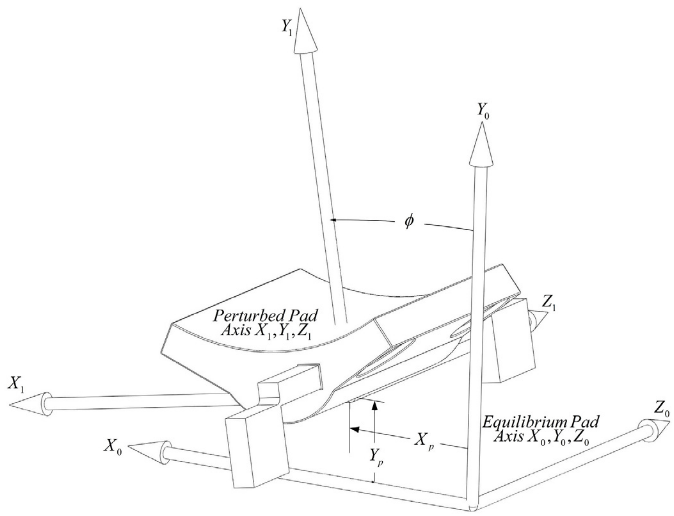

Figure 4: Primary pad degrees of freedom

The orientations of the proximity probes used to measure motion on the loaded pad are illustrated in Figure 5. Each of the five probes (M_{11}-M_{15}) are oriented in the X_0-Y_0 plane shown in Figure 4. Three radial probes (M_{11}-M_{13}) were added in a triangular pattern to observe the tilt, bounce, and pitching motion of the pads, while extensions were added to the sides of the pad to enable two tangential probes (M_{14}, M_{15}) to measure pad slip and yaw motions.

Due to the limited range of motion seen by these probes, small angle assumptions are applied to the geometric relations relating probe measurements to pad degrees of freedom as follows. The tangential motion of the pad is given by

$$X_p = -\frac{(M_{14} + M_{15})}{2}, \tag{15}$$

because the centerline of the proximity probes lies on the contact surface.

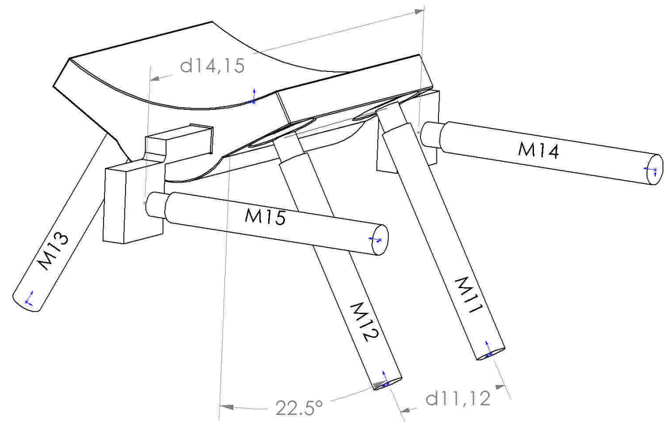

Figure 5: Proximity probe orientation on loaded pad

Their configuration was designed in this manner so that pad tilt is not seen by these probes. The other motion observed by the tangential probes is pad yaw ϕ_{Yp}, defined as a rotation about the positive Y_p-axis according to

$$\phi_{Yp} = \frac{M_{15} - M_{14}}{d_{14,15}}, \tag{16}$$

where the assumption of small motion is justified by the range of motion of the proximity probes. Because the radial pad probes are oriented at an angle of 22.5° from the Y_p-axis, special care must be taken in deriving equations for pad tilt (ϕ), radial motion (Y_p), and pitch (ϕ_{Xp}). Radial motion (Y_p) is defined as the average of vertical motion seen on each side of the pad and is

$$Y_p = \frac{-\left(\frac{M_{11} + M_{12}}{2} + M_{13}\right)}{2} \cos(22.5) \tag{17}$$

Pad pitch is

$$\phi_{X_p} = \left(\frac{M_{12} - M_{11}}{d_{11,12}} + \phi_{Y_p}\right) \cos(22.5), \tag{18}$$

where ϕ_{Yp} negates the effect of yaw on the motion seen by M_{11} and M_{12}. Lastly, pad tilt is

$$\phi = \frac{\left(M_{13} - \frac{M_{11} + M_{12}}{2} - 2X_p \sin(22.5)\right)}{2r_{11} \sin(22.5)} \cos(22.5), \tag{19}$$

where $2r_{11}sin(22.5)$ is the distance from probes M_{11},M_{12} to M_{13} parallel to the X_0-axis, and $2X_p sin(22.5)$ negates the effect of motion in X_p on the relative vertical motion at $M_{11,12}$ and M_{13}. As previously stated, due to the limited 0.46 mm (18 mil) range of motion for these proximity probes, small angle assumptions are valid.

Data Analysis

Writing an equation of motion for the bearing stator and taking an FFT results in

$$m_s \begin{bmatrix} \overline{A}_x \\ \overline{A}_y \end{bmatrix} = \begin{bmatrix} \overline{F}_x \\ \overline{F}_y \end{bmatrix} - \begin{bmatrix} \overline{F}_{bx} \\ \overline{F}_{by} \end{bmatrix}, \tag{20}$$

where A_x and A_y are the absolute stator acceleration components, F_x and F_y are the excitation force components, and F_{bx} and F_{by} are the bearing reaction force components. Rewriting Eq. (20) with the bearing reaction force components represented as impedances yields

$$\begin{bmatrix} \overline{F}_x - m_s\overline{A}_x \\ \overline{F}_y - m_s\overline{A}_y \end{bmatrix} = \begin{bmatrix} \overline{H}_{xx} & \overline{H}_{xy} \\ \overline{H}_{yx} & \overline{H}_{yy} \end{bmatrix} \begin{bmatrix} \overline{U}_{Jx} \\ \overline{U}_{Jx} \end{bmatrix}. \tag{21}$$

To solve Eq. (21), we apply two independent excitations, typically chosen as the orthogonal *X, Y* pair, which provides us with an invertible motion matrix such that the impedances are given by

$$\begin{bmatrix} \overline{F}_{xx} - m_s\overline{A}_{xx} & \overline{F}_{xy} - m_s\overline{A}_{xy} \\ \overline{F}_{yx} - m_s\overline{A}_{yx} & \overline{F}_{yy} - m_s\overline{A}_{yy} \end{bmatrix} \begin{bmatrix} \overline{U}_{Jxx} & \overline{U}_{Jxy} \\ \overline{U}_{Jyx} & \overline{U}_{Jyy} \end{bmatrix}^{-1} = \begin{bmatrix} \overline{H}_{xx} & \overline{H}_{xy} \\ \overline{H}_{yx} & \overline{H}_{yy} \end{bmatrix} \tag{22}$$

If the real portion of $\overline{H}_{ij}$ is quadratic in Ω and the imaginary portion of $\overline{H}_{ij}$ is linear, then the bearing in question can accurately be described by a KCM model such that

$$\mathrm{Re}(\overline{H}_{ij}) = K_{ij} - \omega^2 M_{ij},\ \ \mathrm{Im}(\overline{H}_{ij}) = \omega C_{ij}, \tag{23}$$

where C_{ij} and M_{ij} are determined by the slope of a linear regression in Ω and Ω^2, respectively, and K_{ij} is the intercept of the latter.

To evaluate the measured rotor-pad transfer function from the recorded pad and rotor motions, we employ the same method used to solve Eq. (21), orthogonal excitations. This yields a slightly expanded version of Eq. (11), including the additional pad pitch and yaw motions.

$$\begin{bmatrix} \phi_\eta & \phi_\xi \\ X_{p,\eta} & X_{p,\xi} \\ Y_{p,\eta} & Y_{p,\xi} \\ \phi_{X_p,\eta} & \phi_{X_p,\xi} \\ \phi_{Y_p,\eta} & \phi_{Y_p,\xi} \end{bmatrix} \begin{bmatrix} -\sin(\alpha) & \cos(\alpha) \\ \cos(\alpha) & \sin(\alpha) \end{bmatrix} \begin{bmatrix} \overline{U}_{Jxx} & \overline{U}_{Jxy} \\ \overline{U}_{Jyx} & \overline{U}_{Jyy} \end{bmatrix}^{-1} = \begin{bmatrix} \Gamma_{\phi_\eta} & \Gamma_{\phi_\xi} \\ \Gamma_{X_{p,\eta}} & \Gamma_{X_{p,\xi}} \\ \Gamma_{Y_{p,\eta}} & \Gamma_{Y_{p,\xi}} \\ \Gamma_{\phi_{X_{p,\eta}}} & \Gamma_{\phi_{X_{p,\xi}}} \\ \Gamma_{\phi_{Y_{p,\eta}}} & \Gamma_{\phi_{Y_{p,\xi}}} \end{bmatrix} \tag{24}$$

NUMERICAL PREDICTION

A finite-difference code was developed to solve for the steady-state and dynamic characteristics of a TPJB using the Reynolds equation. Pad and rotor position are determined using a Newton-Raphson algorithm that employs the analytically perturbed fluid-film stiffness and damping matrices. The code allows for each pad's properties to be defined irrespective of the other pads characteristics. This feature includes, but is not limited to, bearing clearance, pad clearance, pad thickness, pad length, offset, thermal properties, etc.

The code does not include a thermal model to determine bearing fluid temperatures and viscosities. To reduce thermal uncertainties, pad surface temperature measurements for each test are used to estimate the circumferential fluid temperature profile on a given pad. This temperature profile is then used to calculate fluid viscosities at each node in the finite-difference grid. Similar measurements showing radial variations in pad temperature are used to estimate thermal bow in the pad, effecting a change in preload and pad radius. An option is also available to account for the temperature-dependent change in bearing clearance due to the mean temperature rise within a given pad.

At 10,000 rpm, the circumferential flow Reynolds number is 384; hence, turbulence can be neglected in the numerical model [17].

The code allows for the input of a polynomial load vs. deflection curve whose derivative describes the static nonlinear stiffness of the pivot. The load-dependent pivot stiffness is used initially to solve for the static equilibrium of the pad, then subsequently in the reduction of dynamic coefficients.

RESULTS

Figure 6 shows the measured load vs. deflection curve of the loaded pad's pivot using two different metrics. The first is the pivot deflection as seen by the relative rotor-stator probes, and the second is the pivot deflection Y_p recorded using the pad probes. The lower stiffness recorded by the rotor-stator probes may be due to the measurement of Babbitt and pad stiffness in series with the pivot stiffness. This assumption supports the use of the stiffer pad measured load deflection curve in the numerical perturbation analysis.

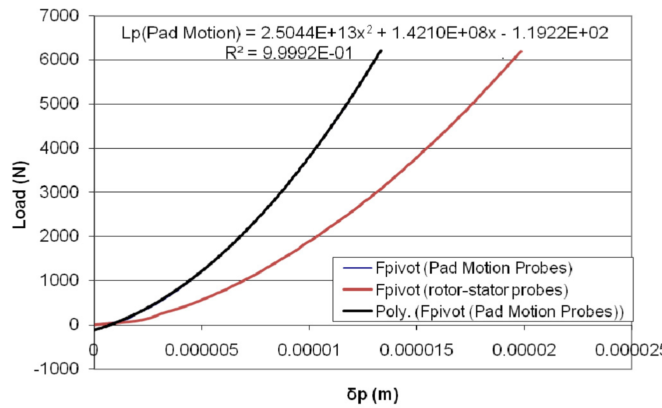

Figure 6: Applied pivot load as a function of measured radial deflection

Figure 7 shows the influence operating temperature has on bearing clearance.

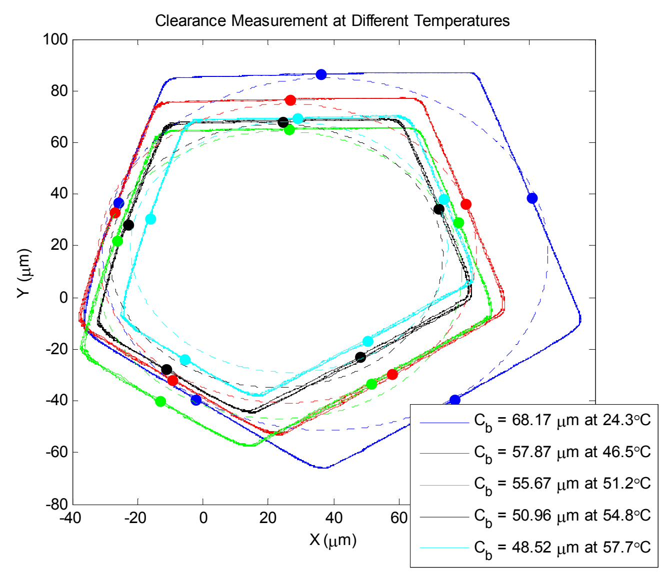

Figure 7: Clearance measurement at a variety of temperatures (as determined by the mean pad temperature within the bearing).

These measurements consist of clearances taken at room temperature, 4400 rpm at low and high loads, and 7200 rpm at low and medium loads, respectively. Clearances are measured by slowly precessing the stator in a circular motion directly after shutting down the test rig after operating at steady state conditions for a given speed and load. These measurements present a very clear picture of the critical geometry within the bearing during a test.

This bearing has five pads, corresponding to the number of sides in the clearance measurement. The top side represents the loaded pad, and shaft rotation is clockwise. At the center of each side, a colored dot represents the pivot location for that pad. Fitting these points to a circle provides an estimate of the best average clearance, which is indicated by the dashed line. At room temperature the clearance is fit well by a circle, indicating that the installed clearance for each pad is very consistent. As the bearing gets hotter, however, the rotor, pads, and bearing begin to expand. Assuming the bearing bore remains constant, a hotter pad will expand more, resulting in a decreased clearance; therefore, the length of that pad's side of the clearance measurement will increase with respect to its peers. If the bearing bore expands more on the hotter side, however, it would tend to increase that pad's clearance and decrease the length of the clearance measurement on that side.

In addition to these relative changes in clearances among the pads, there is significant reduction in the overall clearance in the bearing. Although these are relatively low speeds for a TPJB, the measured clearance following a low-load 7200 rpm test case is 70% of the assembled cold-clearance measurement.

Finally, note that the clearance measurement seems to shift down and to the left with increasing temperature. This effect occurs because the proximity probes taking these measurements are also expanding with temperature. This observation is important because presenting static eccentricity measurements without accounting for the change in probe temperature will result in errors in both eccentricity magnitude and attitude angle. The author believes this is the primary reason for the number of eccentricity measurements presented in literature with slight, but significant, attitude angles. Another option to account for the probe temperature change is to take clearance measurements at each operating condition, and to determine eccentricity ratios based on rotor position within the clearance measurement.

Figures 8-11 show the measured and predicted rotor-pad transfer functions of the loaded pad resulting from the application of Eq. (24) to dynamic measurements for low, medium, and large unit loads at 4400 rpm. In these figures, the pad tilt transfer function Γ_ϕ is non-dimensionalized by multiplying Γ_ϕ by the distance from the pivot to the leading edge of the pad (0.025m). This non-dimensionalization emphasizes the relative importance of ϕ on fluid-film height at the leading/trailing edges of the pad as compared to horizontal and vertical pad motions X_p and Y_p.

Figure 8-A shows the transfer functions resulting from shaft motion in the circumferential (horizontal) axis of the pad as a function of the static load applied to the bearing. The effect of horizontal shaft motion on radial (Y_p) and circumferential (X_p) pad motions are small relative to tilting motion (ϕ), which is effectively tracking the horizontal shaft motion. Assuming that there is no substantial phase lag between the rotor and pad tilt angle, these motions should have little impact on the characteristics of the bearing. Substantial phase lag in this transfer function would suggest that friction may be impeding the tilting motion and causing destabilizing cross-coupled stiffness coefficients.

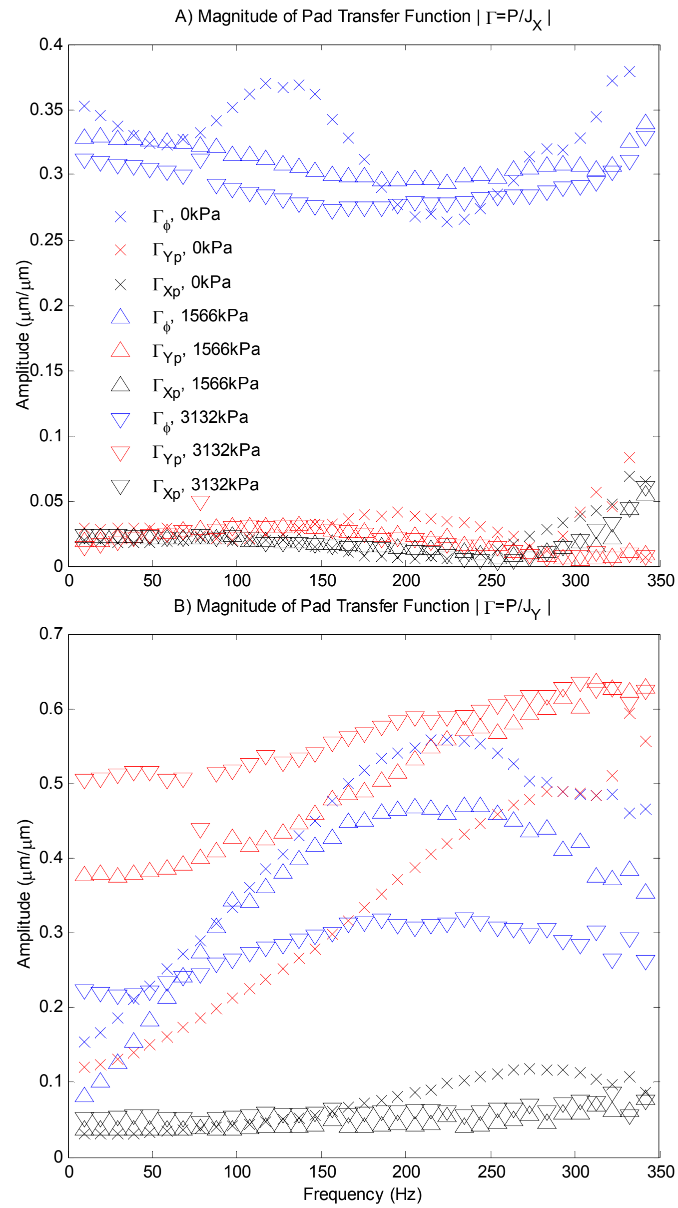

Figure 8: Measured transfer function amplitudes of the loaded pad due to (A) X and (B) Y rotor motions at 4400 rpm with zero, medium and high static bearing loads.

Figure 8-B shows the transfer functions resulting from shaft motion in the radial (vertical) axis of the pad as a function of static load on the bearing. These transfer functions are responsible for direct stiffness and damping coefficients for the bearing, and a good understanding of these transfer functions and how they compare to predictions is vital to correcting modeling deficiencies relating to direct damping and stiffness.

Continuing with Figure 8-B, when unloaded, the tilting motion of the pad accounts for roughly 60% of the change in fluid film height at the pad's leading edge, and radial pad motion in this operating regime comprises approximately 40% of the total motion at the leading edge. As the bearing's static load increases, the relative importance of radial pivot motion on the overall motion of the pad increases significantly;

at a 3132 kPa static bearing load, radial pivot motion comprises more than 70% of the total motion at the leading and trailing edges of the pad. Although the tilting angle affects the convergent shape of the fluid film, which has a dramatic influence on stiffness, radial pivot motion has a substantial impact on both direct stiffness and damping. This impact increases with the load applied to the pad and with frequency of excitation. At large unit loads, the increase in radial pivot motion with frequency is reduced. These observations suggest that including pivot flexibility in a numerical model is mandatory regardless of the loading on the pad, despite increased significance at large unit loads.

Figures 9-11 compare the predicted and measured rotor-pad transfer functions for low, medium, and high bearing static loads. Looking first at the transfer functions resulting from shaft motion in the circumferential (horizontal) axis of the pad shown in Figures 9-11 A, note the following observations. Figure 9-A shows relatively little radial and circumferential motion measured or predicted in comparison to the amount of pad tilt accommodating circumferential rotor motion. The ability of the model to predict the tracking behavior (tilting motion) of the pad is quite good; neither the predicted nor observed tilting motion amplitude changes significantly with load or excitation frequency.

One valuable piece of information can be obtained from this measurement; however, and it relates to the pivot location. Consider the differential force in the tangential direction (dF_η) between the rotor and pad given in Eq (1). If our bearing acts as an ideal tilting pad bearing, then $dF_\eta = 0$, which requires that the perturbed motions $\eta_j = \eta_p = R_{cop}\phi$. Using geometric relations and small angle assumptions, the transfer function between the normalized pad tilting angle and tangential rotor motion should be the distance from the pivot to the leading edge of the pad divided by the distance from the pivot to the center of the pad. For the bearing in question,

$$\Gamma_{\phi_\eta} = \frac{0.025}{R_{co_p}} = 0.363 \qquad (25)$$

which is very close to both the measured and predicted $\Gamma_{\phi\eta}$ shown in Figure 9-A. While R_{cop} would be obvious for the pivot type shown in Figure 1, this simple insight may prove to be more useful for a ball-in-socket or cylindrical pivot, in which the actual pad-pivot location may be in question.

Figures 9-11 B show the transfer functions resulting from shaft motion in the radial (vertical) axis of the pad. Figure 9-B shows that at zero static load, the model predicts radial pad motion amplitudes very accurately throughout the entire frequency range, but fails to reproduce the same accuracy at larger unit loads. Note that the radial pad motion is under-predicted at low loads, and over predicted at high loads. Pad tilt is predicted moderately well at low and high loads, but produces extremely accurate predictions for the medium load case shown in Figure 10-B. There is a substantial degree of circumferential pad (sliding) motion measured at zero unit load in Figure 9-B, while predictions are noticeably smaller. This difference may arise because pad accelerations in the perturbation model assume the rotor is perturbed about a stationary stator, while the stator is perturbed about the rotor in experiments. This perturbation of the stator results in larger pad accelerations that may have some impact on the transfer functions recorded. This said, varying the pad mass and inertia has no discernable impact on the reduced dynamic coefficients predicted, which suggests that both stator and rotor perturbations would produce the same results.

At higher loads, pad sliding motion is smaller and predicted moderately better than at low loads. The effect of sliding motion on the resulting bearing coefficients has not been fully explored, and will be the subject of further research.

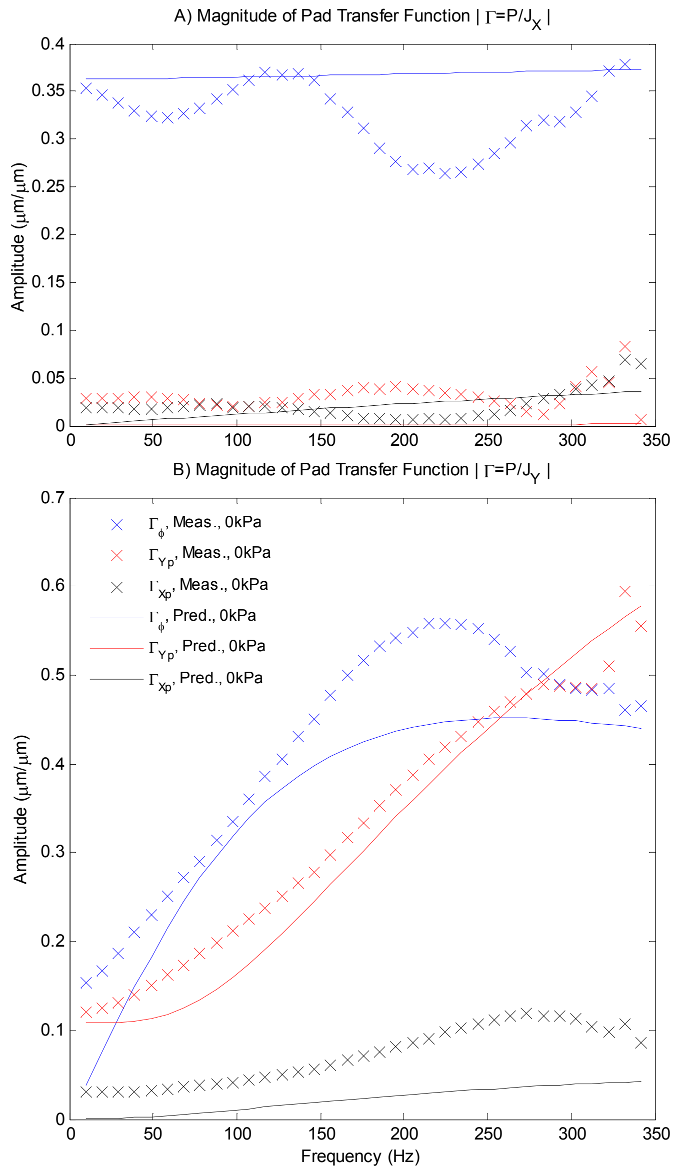

Figure 9: Measured and predicted pad-rotor transfer function amplitudes of the loaded pad due to (A) X and (B) Y rotor motions at 4400 rpm with 0 kPa static bearing load.

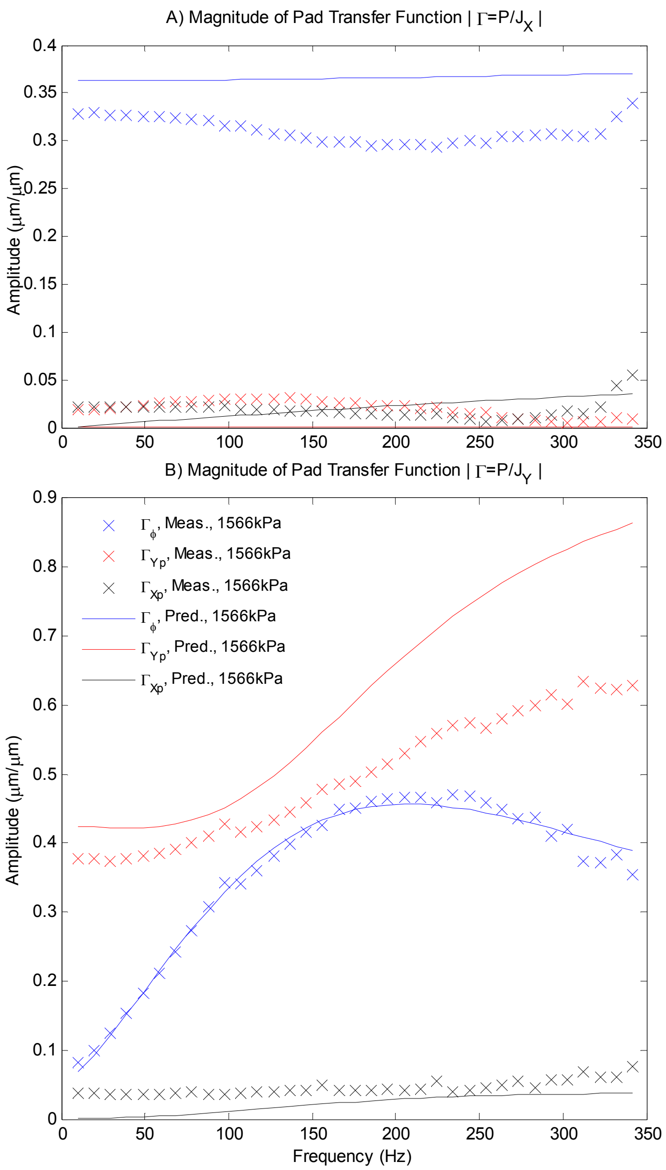

Figure 10: Measured and predicted pad-rotor transfer function amplitudes of the loaded pad due to (A) X and (B) Y rotor motions at 4400 rpm with 1566 kPa static bearing load.

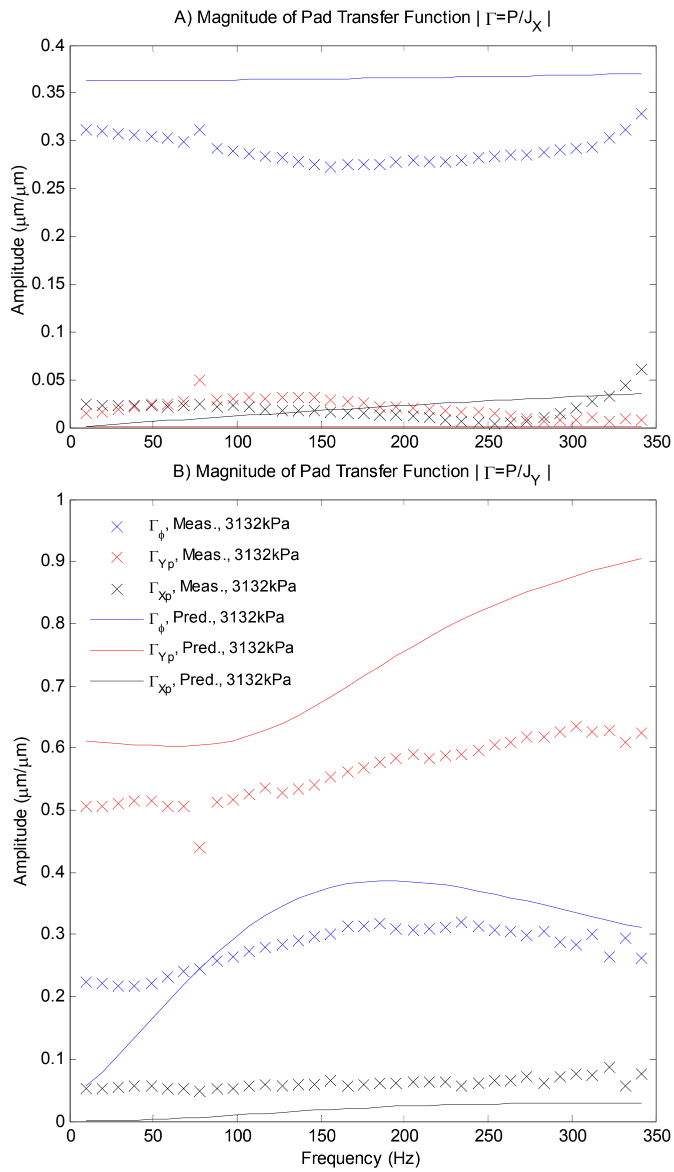

Figure 11 : Measured and predicted pad-rotor transfer function amplitudes of the loaded pad due to (A) X and (B) Y rotor motions at 4400 rpm with 3132 kPa static bearing load.

Figure 12 compares the measured and predicted phase of the pad-rotor transfer function. With the exception of predicted pad vertical motion due to rotor horizontal motion ($\Gamma_{Yp,\eta}$) the phases of the transfer functions are predicted quite well. This holds especially true for the prediction of tilting angle due to vertical rotor motion, which had very accurate amplitude predictions shown in Figure 10. Note the 180° shift in pad sliding phase shown in Figure 12-A. This phase change suggests that at low excitation frequencies, the pad slides in the same direction as the rotor. At higher frequencies, however, the pad slides in the opposite direction of the rotor. This outcome is not predicted by the model, and may be due to the difference in perturbation of the rotor versus the stator mentioned earlier.

Although this seems poor, the author is aware of no papers in literature containing as accurate of damping predictions for heavily loaded bearings at such low speeds. Though space does not permit the inclusion of higher speed test data in this paper, damping coefficients predicted for heavily loaded operation at 10,000 rpm are within 5% of measured values.

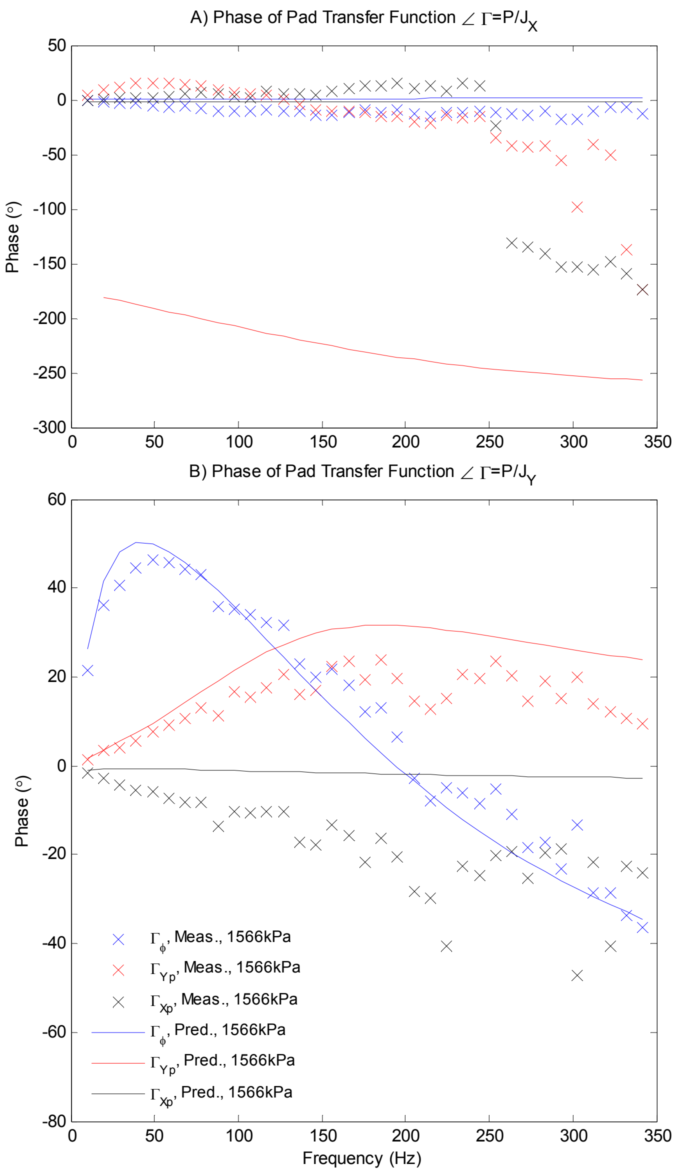

Figure 12: Measured and predicted pad-rotor transfer function amplitudes of the loaded pad due to (A) X and (B) Y rotor motions at 4400 rpm with 1566 kPa static bearing load.

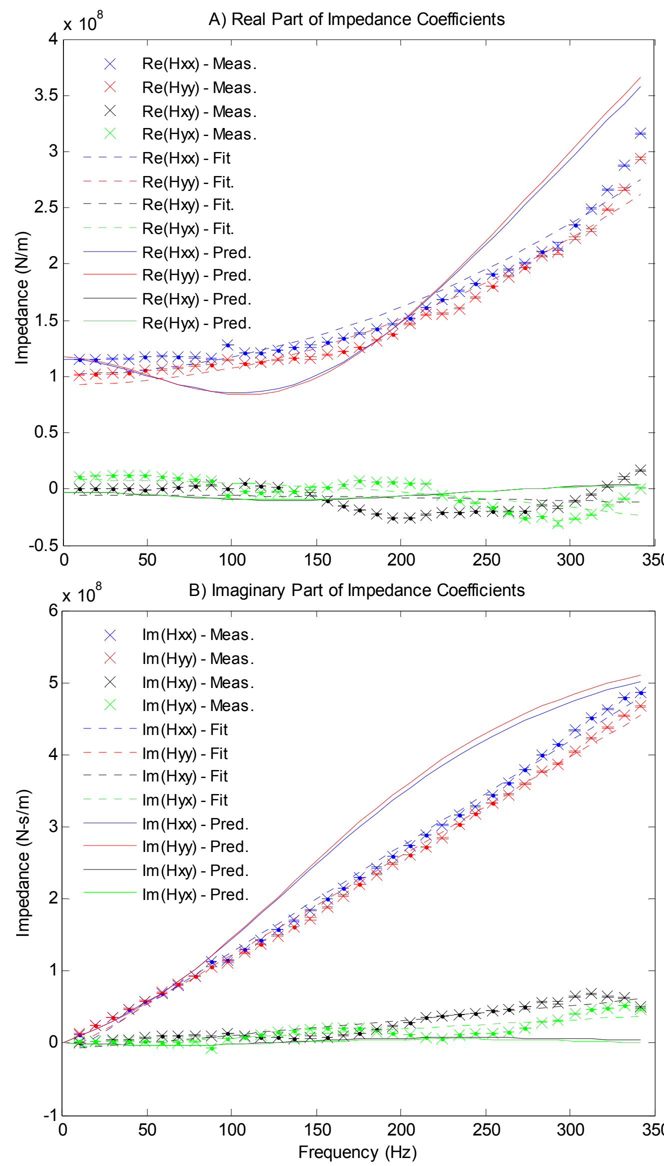

Figure 13: A) Real and B) imaginary components of measured and predicted bearing impedance coefficients at 4400 rpm with 0 kPa static bearing load.

Figures 13-15 show the principal real and imaginary impedances as a function of excitation frequency for low, medium, and large unit loads. These impedances result from the application of Eqs. (20-23) to the test data. The model does well in stiffness and damping prediction at low loads, but deviates moderately in the prediction of direct stiffness H_{yy} at the highest load. Stiffness for this case is over-predicted by 27%. These results are summarized in Table 3, which shows the relative error in predicted stiffness and damping coefficients through running speed at 73Hz. Damping is moderately over-predicted, deviating significantly at frequencies above 100 Hz. If used to determine a damping coefficient through the running speed of 73Hz, it appears that damping prediction would be adequate at low load, but would over-predict damping by 38% at the highest load.

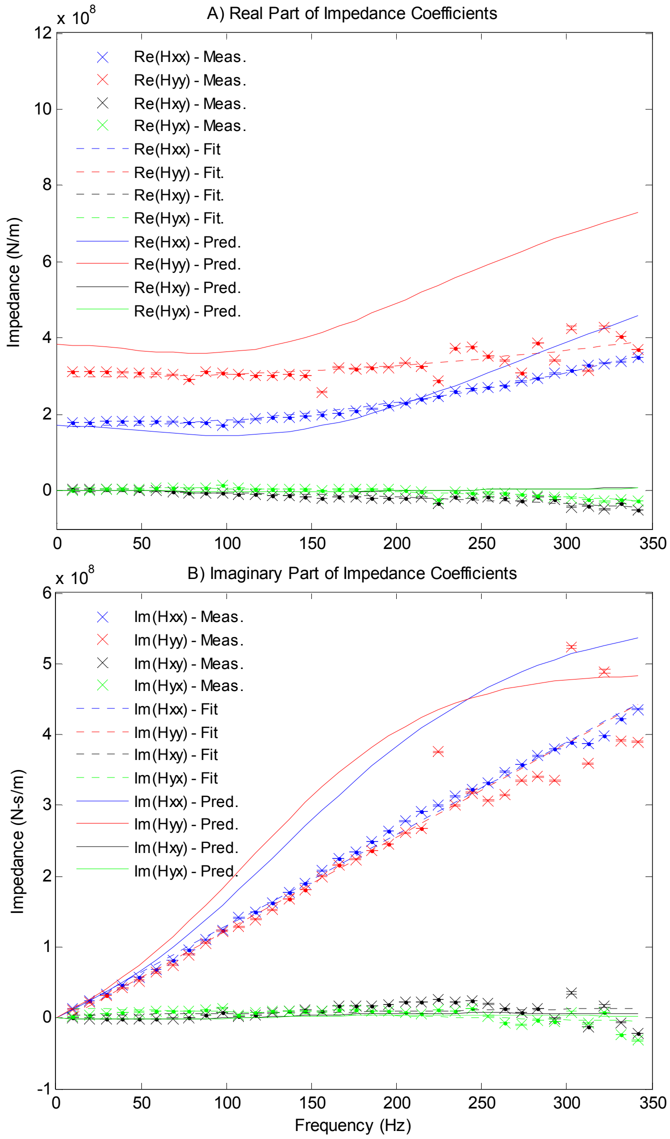

Figure 14: Principal Real and Imaginary H_{ij} at 4400 rpm, 1567 kPa (227 psi) unit load.

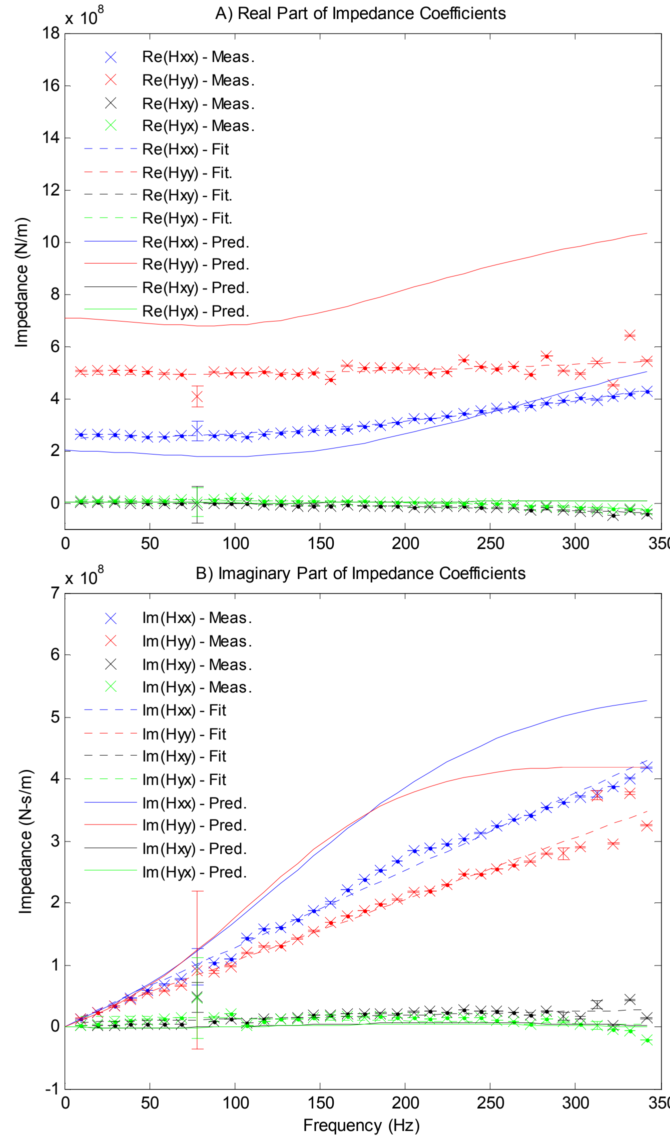

Figure 15: Principal Real and Imaginary H_{ij} at 4400 rpm, 3134 kPa (454 psi) unit load.

Table 3: Percent relative error in principal stiffness and damping coefficients at 4400 rpm (fit through running speed). Positive values indicate overpredicted coefficients.

Load kPa (psi)	$1-\frac{K_{xx,meas}}{K_{xx,pred}}$	$1-\frac{K_{yy,meas}}{K_{yy,pred}}$	$1-\frac{C_{xx,meas}}{C_{xx,pred}}$	$1-\frac{C_{yy,meas}}{C_{yy,pred}}$
0	10.0	21.4	15.0	14.5
1567 (227)	-6.09	17.9	19.0	35.2
3134 (454)	-30.8	27.9	25.4	38.4

SUMMARY AND CONCLUSIONS

A new pad perturbation model is proposed including a tangential degree of freedom for the pad pivot. Perturbations of pad radial and tilting degrees of freedom follows from the analysis initially provided by Lund [1] and Lund and Pederson [2]; however, unlike previous perturbations, this analysis allows for an arbitrary pad center of gravity. This model was implemented in a Reynolds-based TPJB finite-difference code to produce impedance coefficients that were reduced using the general complex root $s=\lambda+j\Omega$. For the prediction of damping coefficients on a harmonically excited test rig, $s=j\Omega$ was implemented to solve for reduced stiffness and damping coefficients.

During the reduction procedure, relations for pad motion as a function of rotor motion were determined at each reduced frequency. The amplitude and phase of these transfer functions were compared to measured pad-rotor transfer functions for tests at low speed over a range of unit loads. Good agreement was found between the amplitude of the measured and predicted transfer functions concerning tilt and radial motions for low to moderate loads, but deviated in accuracy at the highest loaded case.

Circumferential (sliding) pad motion was predicted and observed; however, the author does not assert that the inclusion of a circumferential pad degree of freedom has a substantial impact on bearing coefficients. The effects of these motions on bearing performance were not fully explored, and may provide some insight to pad dynamics in the future.

Note that even on a bearing not classified as having a 'soft pivot', radial motion at high loads can more than double the effect of tilting motion on the fluid-film height at the leading and trailing edges of the pad. The measurements show that predicting TPJB characteristics without accounting for pad pivot deformation is ill advised, regardless of the loading applied to the pivot. For the bearing tested, predictions for direct stiffness and damping compared well to test data at low and moderate loads, but were less accurate when heavily loaded. Direct damping was overpredicted by 38% at the highest load.

Why are damping coefficients over-predicted for the majority of test data? There may be a number of contributing factors. First and foremost may be the notion that accurate prediction of stiffness and static eccentricity characteristics is an alibi for an accurate bearing model. If stiffness and static eccentricity are predicted well, this is not sufficient evidence to dismiss the need for pivot flexibility in the prediction of stiffness and damping coefficients. Several factors can alter the measured stiffness in a test rig if not accounted for. Operating clearance can be reduced to 70% of its cold clearance at 7300 rpm, which has the tendency to increase measured stiffness. In contrast, moving the proximity probes to the side of the stator closest to the stingers reduced measured stiffness by 10-15%, and influenced the frequency dependent behavior of bearing impedances. In the author's perspective, effects such as these have contributed to a lack of confidence in the ability to reliably predict measured stiffness and damping coefficients for the TPJB.

The produced rotor-pad transfer functions can be useful in identifying deficiencies in the model or test setup. The transfer of measured and predicted transfer-function deviations into useful feedback on modeling improvements should be the subject of subsequent work in the field.

ACKNOWLEDGEMENTS

My sincerest gratitude goes out to Chris Kulhanek and Gustavo Vignolo, for helping me to get the test rig in its current condition, to Eddie Denk, who is immensely responsible for the success of the Texas A&M Turbomachinery Laboratory, and to the Turbomachinery Research Consortium (TRC) for sponsoring this research. I would also like to thank my colleagues Dara Childs and Luis SanAndrés for their advice on this subject and the manner in which it is presented.

REFERENCES

[1] Lund, J.W., 1964, "Spring and Damping Coefficients for the Tilting-Pad Journal Bearing," ASLE Trans., **7**, pp. 342-352

[2] Lund, J.W., and Pedersen, L.B., 1987, "The Influence of Pad Flexibility on the Dynamic Coefficients of a Tilting Pad Journal Bearing," ASME J. Trib., **109**(1), pp. 65-70.

[3] Barrett, L. E., Allaire, P. E., and Wilson, B. W., 1988, "The Eigenvalue Dependence of Reduced Tilting Pad Bearing Stiffness and Damping Coefficients," Tribol. Trans., **31**(4), pp. 411-419.

[4] Kirk, R. G., and Reedy, S. W., 1988, "Evaluation of Pivot Stiffness for Typical Tilting-Pad Journal Bearing Designs," J. Vib. Acoust. Stress Reliab. Des., **110**(2), pp. 165-171.

[5] Dmochowski, W., 2006, "Dynamic Properties of Tilting-Pad Journal Bearings: Experimental and Theoretical Investigation of Frequency Effects Due to Pivot Flexibility," Proceedings of ASME Turbo Expo 2006, Paper GT2006-90280, May 8-11, Barcelona, Spain.

[6] Ha, H., and Yang, S., 1999, "Excitation Frequency Effects on the Stiffness and Damping Coefficients of a Five-Pad Tilting Pad Journal Bearing," ASME J. Tribol., **121**, pp. 517-522.

[7] Rodriguez, L., and Childs, D., 2006, "Frequency Dependency of Measured and Predicted Rotordynamic Coefficients for Load-on-Pad Flexible-Pivot Tilting-Pad Bearing," ASME J. Tribol., **128** (2), pp. 388-395.

[8] Carter, C., and Childs, D., 2008 "Measurements versus Predictions for the Rotordynamic Characteristics of a 5-Pad, Rocker-Pivot, Tilting-Pad Bearing in Load Between Pad Configuration," Proceedings of ASME Turbo Expo 2008, Paper GT2008-50069, June 9-13, Berlin, Germany.

[9] Harris, J., and Childs, D., 2008, "Static Performance Characteristics and Rotordynamic Coefficients for a Four-Pad Ball-In-Socket Tiling Pad Journal Bearing," Proceedings of ASME Turbo Expo 2008, Paper GT2008-50063, June 9-13, Berlin, Germany.

[10] Delgado, A., Ertas, B., Drexel M., Naldi, L., and Vannini, G., 2010, "Identification and Prediction of Force Coefficients in a Five-Pad and Four-Pad Tilting Pad Bearing for Load-on-Pad and Load-Between-Pad Configurations," Proceedings of ASME Turbo Expo 2010, Paper GT2010-23802, June 14-18, Glasgow, UK.

[11] Rouvas, C., and Childs, D., 1993, "A parameter Identification Method for the Rotordynamic Coefficients of a High Reynolds Number Hydrostatic Bearing," ASME J. of Vibration and Acoustics, **115**, pp. 264-270.

[12] Kulhanek, C., 2010, "Dynamic and Static Characteristics of a Rocker-Pivot, Tilting-Pad Bearing with 50% and 60% Offsets," M.S. thesis, Mechanical Engineering, Texas A&M University, College Station, TX.

[13] Kulhanek, C., and Childs, D., 2011, "Measured Static and Rotordynamic Coefficient Results for a Rocker-Pivot, Tilting-Pad Bearing with 50 and 60% Offsets, ASME Turbo Expo 2011, Paper GT2010-23802, June 6-10, 2011, Vancouver, Canada.

[14] Sabnavis, G., 2005, "Test Results for Shaft Tracking Behavior of Pads in a Spherical Pivot Type Tilting Pad Journal Bearing," M.S. Thesis, Mechanical Engineering, Virginia Polytechnic Institute and State University, Blacksburg, VA.

[15] Qiao, G., Wang, L., and Zheng, T., 2007. "Linear stability analysis of a tilting-pad journal bearing system". ASME J. Tribol., **129**(2), pp. 348–353.

[16] Glienicke, J., 1966, "Experimental Investigation of Stiffness and Damping Coefficients of Turbine Bearings and Their Application to Instability Predictions," Proceedings of the International Mech. E., **181** (3B), pp. 116-129.

[17] Szeri, A., 1980, "Tribology: friction, lubrication, and wear," Mc Graw Hill Publishing.